Numerical study of chip formation and cutting force in high-speed machining of Ti-6Al-4V bases on finite element modeling with ductile fracture criterion

Mehmet Aydın [1]

Abstract

This paper suggests a novel numerical model to accurately simulate the chip formation for a wide range of high cutting speeds. It consists of finite element (FE) modeling of orthogonal machining of titanium alloy (Ti-6Al-4V) in which the Johnson–Cook (JC) material law which can reflect the strain rate hardening and thermal softening influences, and the JC damage law coupled with the displacement-based ductile failure criterion are implemented during the chip formation. Orthogonal machining simulations are performed in a conventional high cutting speed range of 170 to 250 m/min and at the extreme high cutting speeds ranging from 1200 to 4800 m/min, and saw-tooth chips are occurred. The development of chip serration and cutting force are analyzed. It is found that saw-tooth chip formation in high-speed machining of Ti-6Al-4V is the result of ductile fracture. When the cutting speed is increased from conventional to extreme high speeds, the chip morphology changes with varying the fracture behavior. The numerical model is also verified by comparing predicted results with available experimental data in the literature. The results indicate that chip morphology and cutting force can be accurately acquired using the ductile failure criterion in high-speed machining of Ti-6Al-4V.

Keywords Chip serration · Ductile fracture · High-speed machining · Ti-6Al-4V · Two-dimensional numerical model

Introduction

Ti-6Al-4V is a titanium alloy which is commonly applied to aerospace, automotive and biomedical industries. It has excellent strength maintained at high temperatures, exceptional corrosion resistance and good thermal stability. However, Ti-6Al-4V is difficult to machine, particularly at high cutting speeds, because of its low thermal conductivity and high chemical reactivity [1, 2]. The other noticeable characteristic is the shear localized or saw-tooth chip formation. This phenomenon plays an important role in the cutting force, tool wear and surface integrity of the workpiece during the machining process [3, 4]. To enhance productivity in cutting of Ti-6Al-4V, it is required to investigate the mechanics of the saw-tooth chip formation.

The selection of the flow stress law is important for the accuracy of the cutting simulations. The JC flow stress law [5] has been usually utilized to analyze the cutting process [6–11]. However, the JC law cannot adequately capture the adiabatic phenomenon causing chip serration. This law has been modified by researchers to predict more correctly the behavior of materials at high strain rate. Calamaz et al. [3] suggested a Hyperbolic TANgent (TANH) flow stress law by adding a term to the JC law to account for strain softening, and successfully simulated saw-tooth chip formation in cutting of Ti-6Al-4V at low cutting speeds. Then, they enhanced the strain softening model by including temperature [12] and strain-rate effects [13]. Sima and Özel [14] developed the TANH material law by introducing the temperature-dependent flow softening. Further, analytical methods were suggested to establish JC constants from the mechanics of the cutting process [15, 16].

In most situations, the saw-tooth chip is formed by the application of a failure criterion to the simulation. Umbrello [17] studied three different sets of JC coefficients with Cockroft and Latham's criterion to describe the chip geometry in cutting Ti-6Al-4V. Subbiah and Melkote [18] demonstrated the ductile tearing phenomenon in front of the tool tip in

✉ Mehmet Aydın
 mehmet.aydin@bilecik.edu.tr

[1] Bilecik Şeyh Edebali University, Industrial Design, 11230 Bilecik, Turkey

microcutting experiments on aluminum alloy and implemented a ductile shear failure criterion to numerical model. Owen and Vaz [19] implemented a ductile failure criterion to high-speed machining in adiabatic strain localization conditions, and described the material failure through a failure softening phenomenon. Wang and Liu [20] proposed a numerical and experimental approach for high-speed cutting simulation of Ti-6Al-4V by considering an energy-based failure criterion. Ambati and Yuan [21] used a plastic displacement failure criterion with exponential softening to study the effect of element size for cutting process simulations. Mabrouki et al. [22] gave a definition of the failure energy for cutting simulation of aluminum alloy A2024-T351, which was associated with characteristic element length. Zhang et al. [23] enhanced the tool-chip friction model using a FE machining model including the energy-based fracture criterion.

The saw-tooth chip formation is still not properly known, which is seen in a particular range of cutting speed. Nevertheless, two mechanisms are recognized: (I) thermoplastic instability mechanism and (II) crack growth inside the primary shear zone (PSZ). Molinari et al. [1] proposed a thermomechanical instability approach to study the dependency of the shear deformation patterning to the cutting speed. Hua and Shivpuri [24] observed that chip serration was because of a ductile fracture occurring during machining process. This phenomenon was related to the crack growth in the PSZ. Sutter and List [25] stated that the shear localization and fracture mechanisms dominated chip formation at high-speed cutting of Ti-6Al-4V. While most research studies have been published to study the saw-tooth chip formation, which involve experimental [26, 27], theoretical [28, 29] and numerical [30–33], there are a few accurate researches regarding FE analysis including the determination of both chip morphology and cutting force, particularly in high-speed machining. To identify with a high accuracy both chip morphology and force especially in cutting of Ti-6Al-4V using numerical methods under different high-speed machining conditions, it is needed to establish a suitable numerical model, which can allow more physical insights into the saw-tooth chip formation mechanism.

This paper presents the contribution to the research of physical phenomena causing saw-tooth chip during high-speed machining. A novel FE-based numerical model of orthogonal machining is suggested to accurately analyze the chip formation over a wide range of high cutting speeds. To improve the numerical model quality, the JC damage model with the displacement-based ductile failure criterion is employed along with the JC flow stress law. This approach is applied to characterize the chip morphology and cutting force in cutting of Ti-6Al-4V. The numerical predictions are compared with the values acquired from experimental studies found in the literature for the studied tool-workpiece couple. The FE model provides considerably the prediction of saw-tooth chips by crack formation under shear deformation.

Development of numerical model of orthogonal machining

A two-dimensional plane-strain model of the orthogonal machining was developed with the aid of the FE software ABAQUS/Explicit. A temperature-displacement procedure was chosen for modeling of high-speed machining.

Basic settings of the model

Figure 1 illustrates the numerical model developed for the orthogonal machining simulations. The workpiece was consisted of three parts: (1) chip, (2) parting line, (3) workpiece base. These parts were joined by implementing the tie constraint. The parting line was used to provide the chip separation through the element deletion. Damage criterion was defined to chip and parting line whereas damage was not implemented to workpiece base. The dimensions of workpiece geometry were defined in terms of feed (f). The ratio of f to h was 1:4, whereas the ratio of f to l was 1:10.

A four-node quadrilateral elements (CPE4RT) were utilized to mesh the cutting tool and workpiece. All parts of the workpiece were the same element properties, except that enhanced hourglass control and the distortion length ratio of 0.08 were applied to the chip where large plastic deformation happens. The chip was defined by twelve layers having 125 elements in each layer. The chip elements were backward-inclined of 45° to avoid the severe distortion of the elements caused by the intense compression, shear strain and surface friction when the chip separates from the workpiece and comes in contact with the tool. In addition, one layer of elements with a height equal to one twentieth of feed was used to model the parting line. The cutting edge radius (r) was also equal to the thickness of parting line. Ten layers of elements were applied to the workpiece base under the cutting surface. A non-uniform mesh was employed for the rigid cutting tool.

The kinematic constraints of the cutting tool were assigned by a reference node. The tool would move horizontally from right to left whereas constrained in vertical direction. The bottom, right and left surfaces of the workpiece base were constant to prevent the movement of the workpiece during machining. A starting temperature of 293 K was also implemented to the FE model.

The numerical process model was suggested by keeping constant the intensity of failure. There were three main properties of this model: (1) JC damage law with the displacement-based ductile failure criterion was applied along with the JC material law; (2) Uniform mesh was generated without remeshing technique; (3) The numerical model was calibrated by adjusting the failure criterion based on characteristic length (L) at a cutting condition, and then used in a wide range of conditions.

Fig. 1 Geometry of numerical model
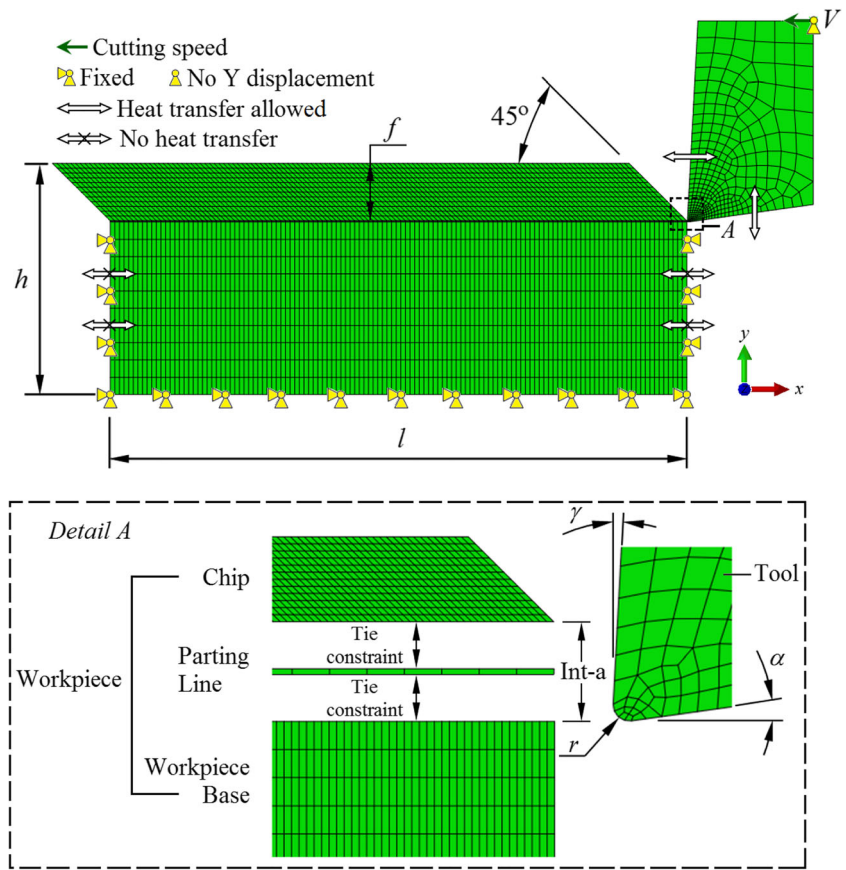
Material constitutive law

To describe the constitutive behaviour of Ti-6Al-4V, the JC material law was applied, which is denoted by

$$\overline{\sigma} = \left[A + B\left(\overline{\varepsilon}^{pl}\right)^n\right]\left[1 + CIn\left(\overline{\dot{\varepsilon}}^{pl}/\dot{\overline{\varepsilon}}_0\right)\right]\left[1 - \left(\frac{T - T_{room}}{T_{melt} - T_{room}}\right)^m\right] \quad (1)$$

where $\overline{\sigma}$ is the flow stress, $\overline{\varepsilon}^{pl}$ is the plastic strain, $\overline{\dot{\varepsilon}}^{pl}$ is the strain rate (s^{-1}), $\dot{\overline{\varepsilon}}_0$ is the reference strain rate (1.0 s^{-1}). The parameters T, T_{room} (293 K) and T_{melt} (1878 K) are workpiece temperature, room temperature, material melting temperature, respectively. The JC material constants of Ti-6Al-4V are reported in Table 1, while the workpiece and cutting tool properties are presented in Table 2.

Chip formation criterion

A two-stage ductile failure/damage law was used to model chip formation, i.e., The initial stage includes the damage initiation whereas the latter includes damage evolution, as shown in Fig. 2. At the first stage (a–b), material is linear elastic. The material passes the plastic deformation stage (b–c) with strain hardening when the stress reaches the yield stress σ_y, where the curve (c-d′) represents the undamaged stress–strain (σ–ε) behavior. Point c corresponds the material status at the damage beginning, namely the damage initiation criterion. Afterward, material goes the damage evolution stage (c–d) in which the thermal softening becomes further apparent. When the curve σ–ε approaches to point d, its stiffness is entirely degraded and the fracture emerges as an indication of failure [20].

Damage initiation

Johnson [36] proposed the following JC damage law to simulate the chip separation from the workpiece, which is utilized as damage initiation criterion.

Table 1 JC constants of Ti-6Al-4V [34]

Initial yield strength	A (MPa)	862
Hardening modulus	B (MPa)	331
Strain rate sensitivity coefficient	C	0.012
Strain hardening coefficient	n	0.34
Thermal softening coefficient	m	0.8

Table 2 Workpiece and cutting tool properties [7, 35]

	Workpiece (Ti-6Al-4V)	Tool (tungsten carbide)
Density (Kg/m^3)	4430	11,900
Young's modulus (GPa)	109 (323 K) 91 (523 K) 75 (723 K)	534
Poisson's ratio	0.34	0.22
Thermal expansion coefficient (1/K)	9×10^{-6}	
Conductivity (W/m°K)	6.8 (293 K) 7.4 (373 K) 9.8 (573 K) 11.8 (773 K)	50
Specific heat (J/Kg°K)	611 (293 K) 624 (373 K) 674 (573 K) 703 (773 K)	400

Table 3 JC failure parameters of Ti-6Al-4V [34]

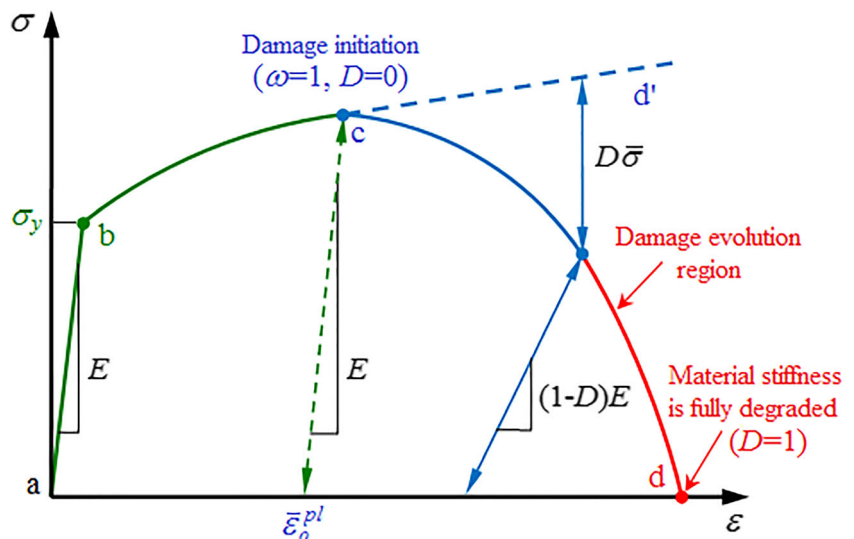| Initial failure strain	d_1	−0.09
Exponential factor	d_2	0.25
Triaxiality factor	d_3	−0.5
Strain rate factor	d_4	0.014
Temperature factor	d_5	3.87

$$\overline{\varepsilon}_o^{pl} = \left[d_1 + d_2 \exp\left(d_3 \frac{p}{\overline{\sigma}} \right) \right] \left[1 + d_4 \ln\left(\frac{\dot{\overline{\varepsilon}}^{pl}}{\dot{\overline{\varepsilon}}_0} \right) \right] \left[1 + d_5 \left(\frac{T - T_{room}}{T_{melt} - T_{room}} \right) \right] \tag{2}$$

where p is the hydrostatic pressure. The ratio of $p/\overline{\sigma}$ denotes the stress triaxiality. The plastic strain at the beginning of damage $\overline{\varepsilon}_o^{pl}$ depends on the stress triaxiality, strain rate, temperature and JC failure parameters ($d_1 \sim d_5$) presented in Table 3.

The damage is allowed to initiate when a scalar state variable ω approaches 1. The variable ω is expressed by

$$\omega = \sum_{j=1}^{n} \left(\frac{\Delta \overline{\varepsilon}^{pl}}{\overline{\varepsilon}_o^{pl}} \right)_j \tag{3}$$

where $\Delta \overline{\varepsilon}^{pl}$ is the increment of the strain during loading j.

Damage evolution

A displacement-based ductile failure criterion was assigned to define the damage evolution. This criterion includes the plastic displacement $\left(\overline{u}^{pl} \right)$ as a failure parameter which represents the energy necessary to occur a unit area of crack.

The ductile damage evolution criterion is given by Eq. (4), which ensures a linear softening.

$$\overline{u}^{pl} = L \overline{\varepsilon}^{pl} \tag{4}$$

where L is the characteristic element length and assumed as the square root of the integral area. In Eq. (4), the strain is inversely proportional to the mesh dimension. Accordingly, the implementation of the plastic displacement $\left(\overline{u}^{pl} \right)$ mitigates the mesh dimension dependency.

The damage variable (D) can be represented as

$$D = \frac{\overline{u}^{pl}}{\overline{u}_f^{pl}} = \frac{L \overline{\varepsilon}^{pl}}{\overline{u}_f^{pl}} \tag{5}$$

where the element in the damage zone is totally degraded ($D = 1$) when $\left(\overline{u}^{pl} \right)$ approaches the failure plastic displacement $\left(\overline{u}_f^{pl} \right)$.

Fig. 2 Stress–strain curve

Tool-chip interface

The tool-chip interaction is defined by modeling the frictional (τ_f) and normal (σ_n) stresses [37].

As commonly known, a sticking region occurs at the interface, and the frictional shear stress in this region (τ_f) corresponds to the equivalent shear stress (k_{chip}). Along the rest of the interface, a sliding happens, and τ_f can be found from a friction coefficient (μ). This Coulomb friction law can be stated by

$$\tau_f = \begin{cases} \mu \times \sigma_n & \text{If } \mu \times \sigma_n < k_{chip}(\text{sliding}) \\ k_{chip} & \text{If } \mu \times \sigma_n \geq k_{chip}(\text{sliding}) \end{cases} \quad (6)$$

In this study, the relationship between tool-chip contact pair was defined through penalty contact algorithm, in which the cutting tool was the master surface whereas the chip was the slave. To manage the friction at the interface during saw-tooth chip simulations, the friction coefficient was taken as 0.05 from Ref. [3] for the same tool-workpiece material combination. Thermal boundary conditions were applied to perform heat transfer. The thermal conductance was adjusted to an extremely high value of 10^7 W/m²°K, based on Refs. [38, 39].

The surface-to-surface contact method and the penalty contact algorithm were also applied to the contact pair (Int-a) between the surfaces of the chip and workpiece base in order to prevent element penetration. Friction in this contact was neglected. "Hard" contact was employed to describe the normal behavior of this contact pair.

Heat generation

The heat arises from plastic deformation and friction. The heat flux $\left(\dot{q}_p\right)$ caused by plastic deformation is calculated from

$$\dot{q}_p = \eta_p \overline{\sigma} \dot{\overline{\varepsilon}}^{pl} \quad (7)$$

where η_p is the inelastic heat fraction that is assumed as 0.9.

The frictional heat flux $\left(\dot{q}_f\right)$ can be stated as

$$\dot{q}_f = \eta_f \tau_f V_c \quad (8)$$

where η_f is the fraction of energy produced due to friction and taken as 1. V_c is the chip sliding velocity. The frictional thermal energy is partitioned between the chip and tool surfaces by

$$\dot{q}_{\rightarrow chip} = f_f \dot{q}_f \text{ and } \dot{q}_{\rightarrow tool} = \left(1 - f_f\right) \dot{q}_f \quad (9)$$

where $\dot{q}_{\rightarrow chip}$ and $\dot{q}_{\rightarrow tool}$ are the heat flux per unit area flowing to chip and tool, respectively, and f_f is the weighting factor and taken as 0.6 here.

Fe simulation in conventional high-speed machining

Experimental reference

Machining is a complex three-dimensional process which involves many phenomena. Thus, for simplicity, orthogonal machining is commonly used [26]. An orthogonal machining configuration was introduced in Ref. [7]. It comprises of removing the top layer of the workpiece with a feed of the tool toward the workpiece, as presented in Fig. 3. The machined feature is a disc with 100 mm diameter × 2.03 mm thickness held on the spindle of machine tool.

In order to compare the numerical cutting forces and the chip morphologies with experimental results for conventional high cutting speeds in the range $170 \leq V \leq 250$ m/min, the orthogonal machining model employs the same cutting parameters as the reference study of Chen et al. [7]. These authors conducted orthogonally the cutting experiments on a vertical machining center. The workpiece material was Ti-6Al-4V alloy. The cutting tool was a fresh uncoated TPGN110304 carbide insert in grade of KCU10, manufactured by Kennametal. The principal cutting force (F_c) was measured with a Kistler type 9257A three-dimensional dynamometer in dry condition. The cutting parameters are presented in Table 4.

Chip formation and morphology

The chip serration is an elementary characteristic of Ti-6Al-4V in high-speed machining. Figure 4 illustrates the different times (t) of the chip serration at the conventional high cutting speed of 170 m/min. It was seen in Fig. 4(a) that the periodic fracture was initiated at the outer surface of the chip when the scalar stiffness degradation (SDEG) was greater than 0.94. Then, it advanced down toward the tool tip in the PSZ until the compressive stresses occurred from the tool tip were large enough to stop the crack, thus completing the initial segment of the saw-tooth chip, namely shear-localized chip. This was followed by a new shear band production and crack growth, finally causing a second segment (Fig. 4(b)–(d)). The process reproduced itself continually and caused the shear-localized chip morphology. The bending of the newly formed chip segments moving along the secondary shear zone (SSZ) was also seen in the tool movement direction because of the joint strength degradation between segments.

In machining of Ti-6Al-4V, the saw-tooth chip is generally occurred through the thermoplastic shear mechanism. It was clearly evident from numerical simulation in the present study that at high cutting speeds, failure was taken place by ductile fracture, obviously indicating the thermal softening in the PSZ.

Fig. 3 Orthogonal machining configuration [7]
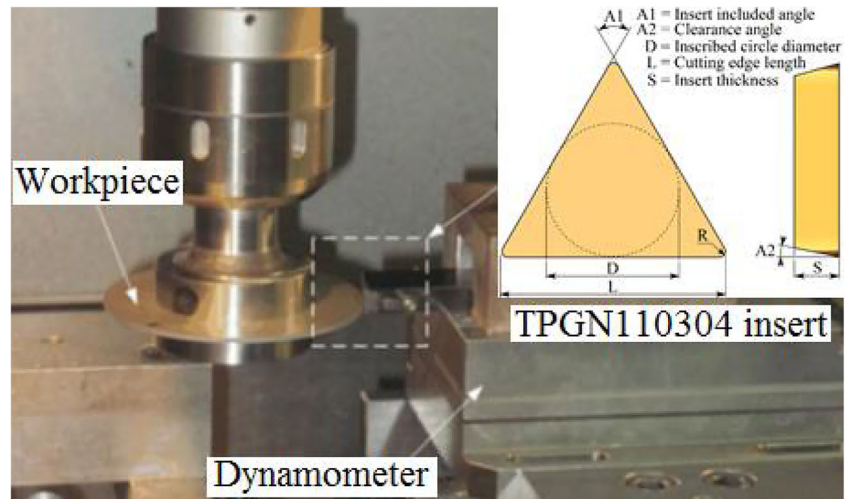
Geometric characteristics of saw-tooth chips

The geometric characteristics of saw-tooth chips are defined through their dimensional values in terms of pitch, peak and valley. Chip segments are taken place periodically on the whole chip. Therefore, the second and third etc. are approximately the similar shape and dimension.

Figures 5, 6, 7, 8 illustrates the experimentally obtained [7] and numerically calculated chip morphologies in the range of conventional high speeds $170 \leq V \leq 250$ m/min. It was observed that the numerical segment shape was not completely the same as the actual segment (Fig. 6). However, the global morphologies of the numerical chips were fairly similar to those given in the experimental study for conventional high cutting speeds.

The above mentioned figures also illustrate the equivalent plastic strain (PEEQ) distributions which help understanding the chip formation mechanism. The high strains were occurred in the PSZ and SSZ, indicating that the material undergoes severe shear localization. The high plastic strains coincided with approximately the shear plane. The scale of PEEQ was constant at about 6 for the simulations. The PEEQ in shear bands approximately changed from 2 to 4 at conventional high cutting speeds. Besides, the shear bands became wider from the external chip surface to the chip root because of the tool-chip friction. The plastic deformation tendency also can be

obviously seen in actual chip morphologies, as presented in Figs. 6 and 8.

The geometrical dimensions of the predicted chip were measured four times at each cutting condition to minimize measurement errors, and the average value of measurements was taken into account here. Table 5 shows the numerical results and those acquired experimentally in terms of peak, valley and pitch for conventional high-speed machining conditions 1–3. It was found that the differences between the peak heights of numerical and experimental chips were 9.3%, 14.6% and 14.5% for conditions 1–3, respectively. Along the cutting speed range studied, the predicted peak heights agreed very well with those observed in actual cutting processes. The most difficult chip parameter for the calculation through simulations was the valley height. In conventional high-speed machining, this parameter was underestimated with differences less than 10%. The differences between the numerical and experimental segment pitches were 13.3%, 27.8% and 16% for conditions 1–3, respectively. That is, the differences between the segment pitches were not more than about 15%, except for condition 2.

In general, actual chip dimensions are determined at room temperature after entirely delivering the elastic deformation, however the numerical chip partly delivers the elastic deformation. Accordingly, the actual chip has larger dimensions of peak, valley and pitch.

Table 4 Cutting conditions and tool geometry

Cutting conditions	Cutting speed, V (m/min)	Feed, f (μm/rev)	Depth of cut, a_p (mm)	Rake angle, γ (°)	Clearance angle, α (°)	Cutting edge radius, r (μm)
1	210	100				
2	250	100	2.03	3	8	5
3	170	120				
4	170	150				

Fig. 4 Chip serration of Ti-6Al-4V at $V = 170$ m/min and $f = 120$ μm/rev: (a) $t = 5.088 \times 10^{-5}$ s; (b) $t = 5.512 \times 10^{-5}$ s; (c) $t = 7.844 \times 10^{-5}$ s; (d) $t = 8.692 \times 10^{-5}$ s
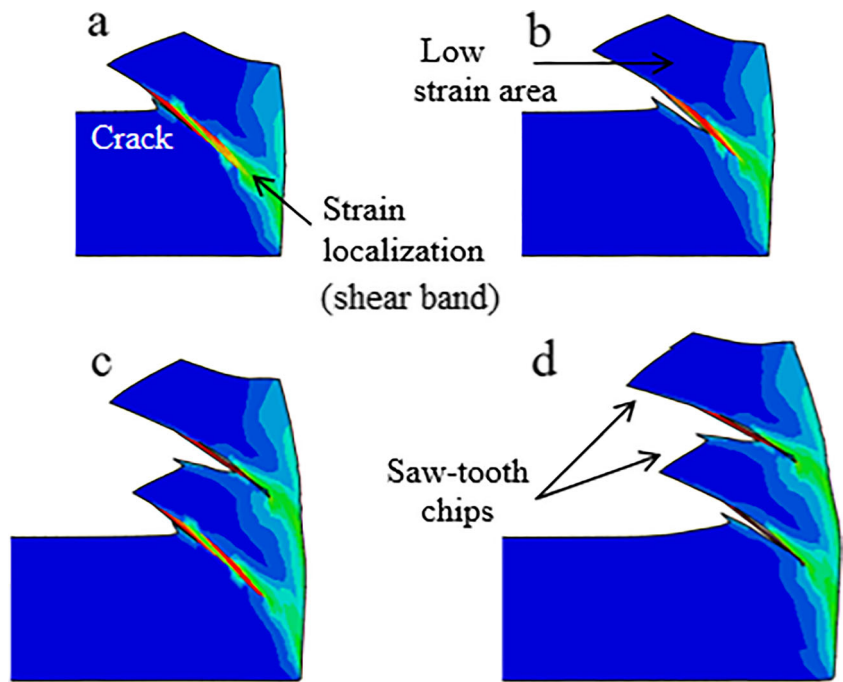
The saw-tooth chip is described as a sequence of trapezoids occurred through two shearing planes. By considering the tooth pitch (p_c) and the chip velocity (V_c), the frequency of saw-tooth chip (f_c) can be approximated by [40].

$$f_c(kHZ) = \frac{V_c(\text{m/s})}{p_c(\text{mm})} \quad (10)$$
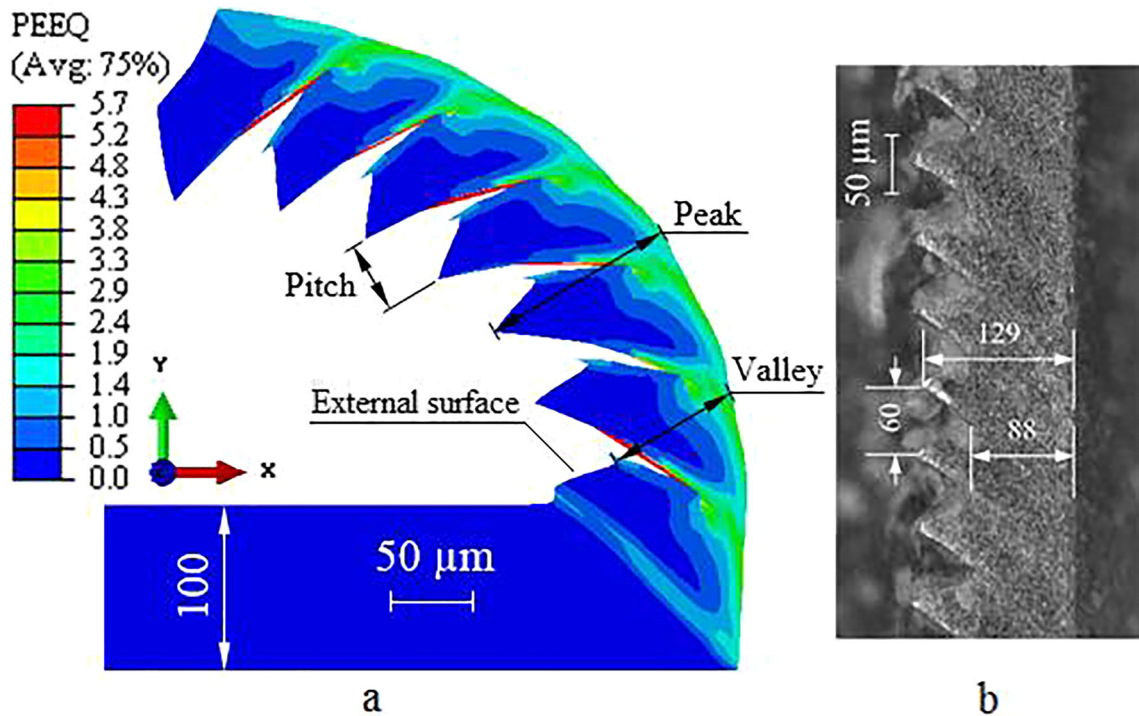
Fig. 5 Chip morphology of Ti-6Al-4V acquired for orthogonal machining at $V = 210$ m/min and $f = 100$ μm/rev: (a) numerical; (b) experimental [7]
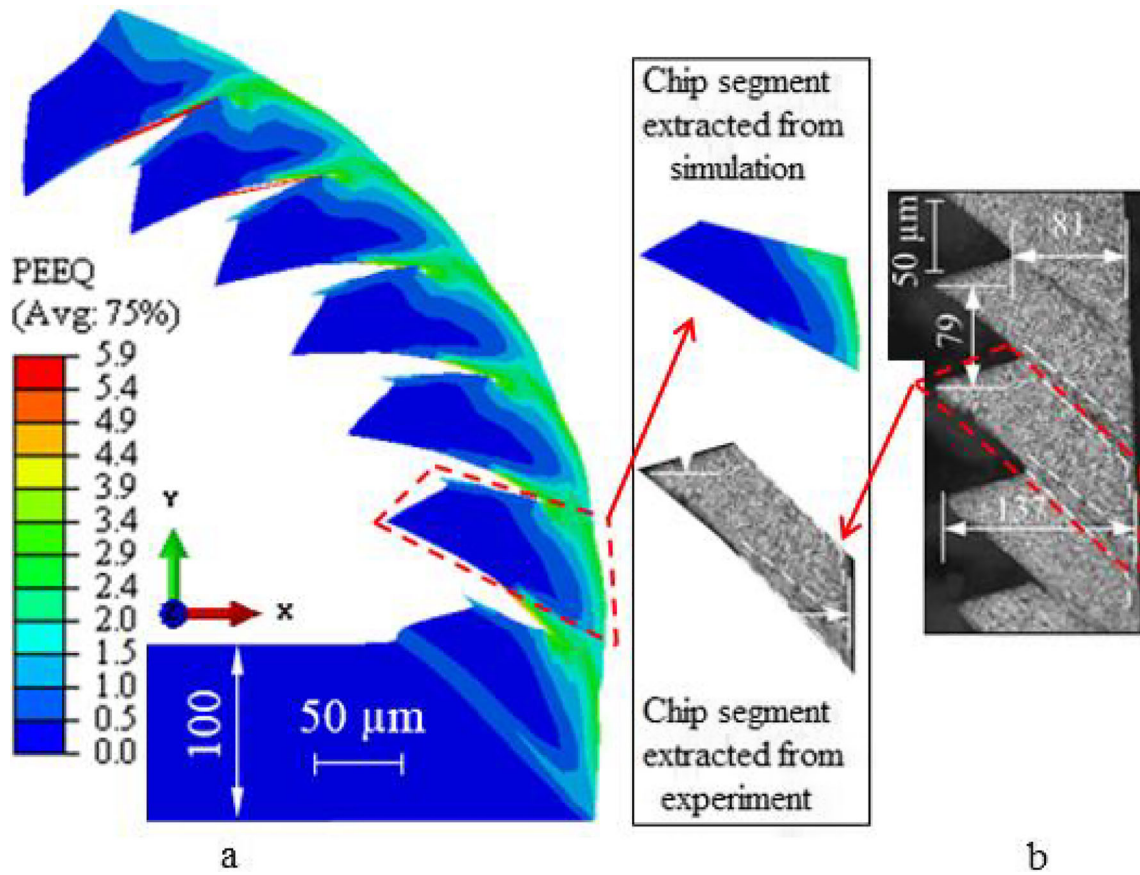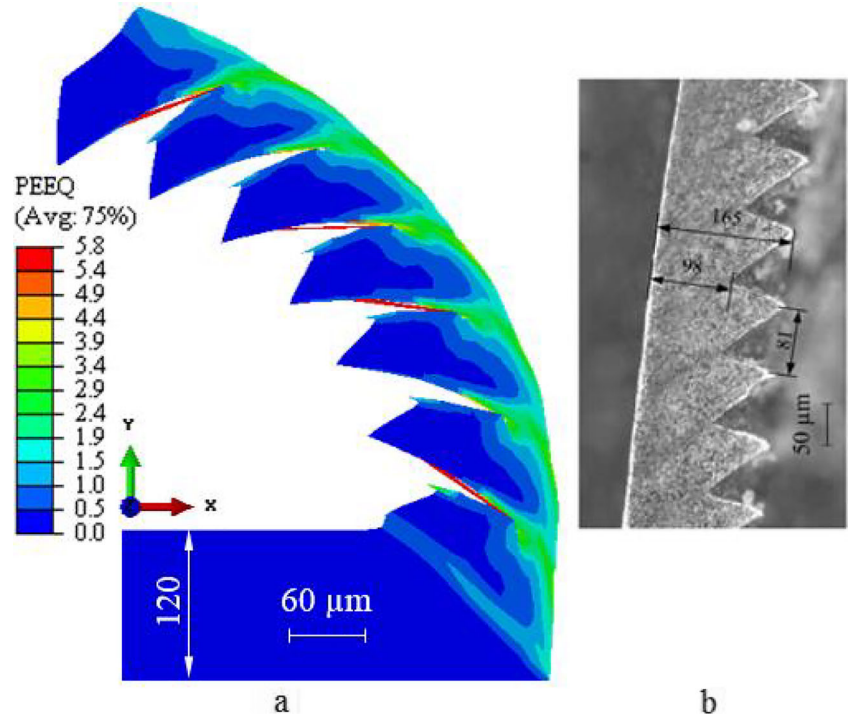
Fig. 6 Chip morphology of Ti-6Al-4V acquired for orthogonal machining at $V = 250$ m/min and $f = 100$ μm/rev: (a) numerical; (b) experimental [7]

Fig. 7 Chip morphology of Ti-6Al-4V acquired for orthogonal machining at $V = 170$ m/min and $f = 120$ μm/rev: (a) numerical; (b) experimental [7]

Fig. 8 Chip morphology of Ti-6Al-4V acquired for orthogonal machining at $V = 170$ m/min and $f = 150$ μm/rev: (a) numerical; (b) experimental [7]
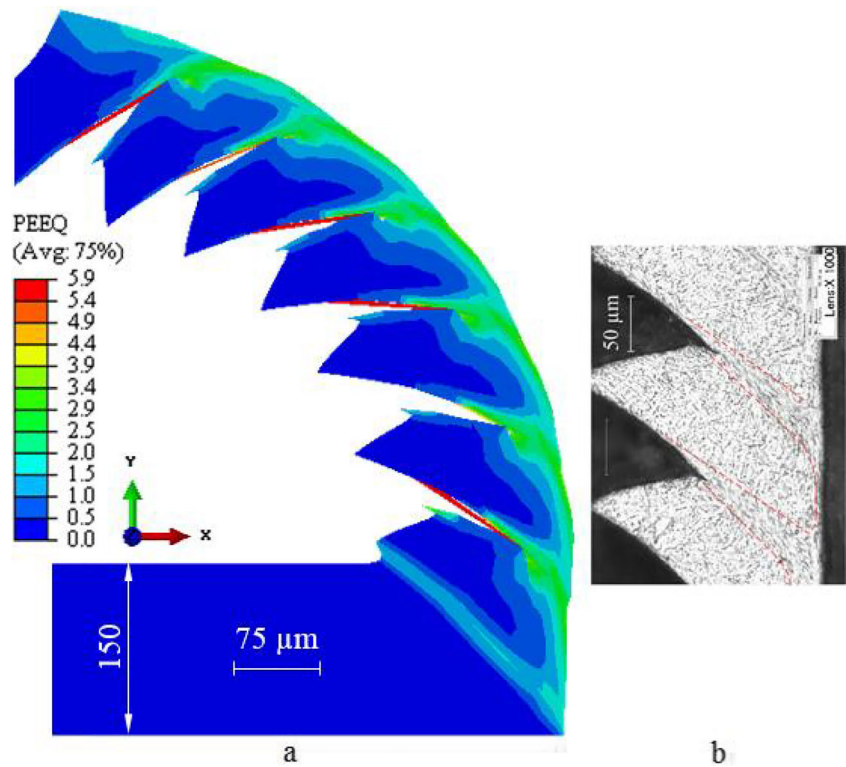
The parameter f_c values for conventional high-speed machining conditions are presented in Table 5. It was observed from the numerical results that parameter f_c increased with increasing cutting speed. Besides, the numerical f_c values matched well with the experimental results.

Cutting force

In the case of a cutting speed of 210 m/min and feed of 100 μm/rev, the variation in the numerical force F_c with cutting time is presented in Fig. 9. It was found that the force F_c fluctuated in two manners. The first can be associated with fluctuations of small periods which correspond to a numerical distribution.

The second matches a higher period and it is the result of chip serration that reduces the material removal rate and tool life.

The average numerical and experimental [7] forces F_c are presented in Fig. 10. The force F_c remained approximately constant with an increase of the cutting speed from 210 to 250 m/min at the feed of 100 μm/rev, such as conditions 1 and 2. As seen clearly from the numerical data, a slight decrease in the cutting force was also predicted when the cutting speed increased. This tendency acquired through the model demonstrates the increasing temperature of the PSZ causing a lower force.

In machining of Ti-6Al-4V, there was a considerable increase of the cutting force with increasing feed from

Table 5 Comparison between the characteristics of numerical and experimental [7] chips in conventional high-speed machining

Cutting Conditions		Chip morphology (μm)			Frequency, f_c (kHz)
		Valley	Peak	Pitch	
Test 1 $V=210$ m/min	Experimental	88	129	60	75
$f=100$ μm/rev	Numerical	81	117	52	78
	Difference	8%	9.3%	13.3%	-4%
Test 2	Experimental	81	137	79	72
$V=250$ m/min	Numerical	80	117	57	85
$f=100$ μm/rev	Difference	1.2%	14.6%	27.8%	−18.1%
Test 3	Experimental	98	165	81	48
$V=170$ m/min	Numerical	97	141	68	49
$f=120$ μm/rev	Difference	1%	14.5%	16%	−2.1%
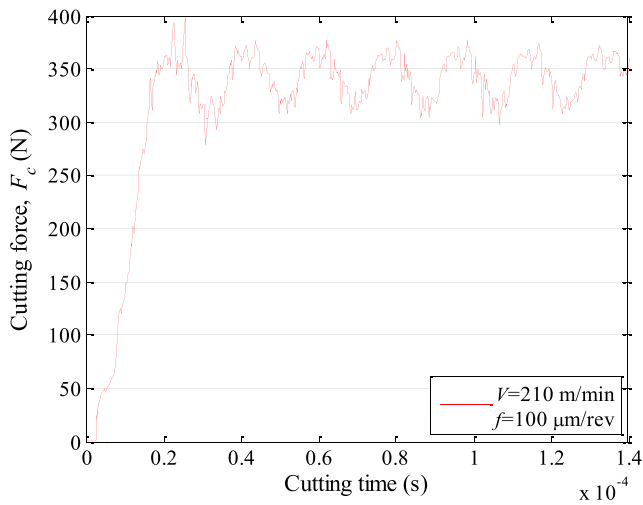
Fig. 9 Variation in the numerical force F_c with time ($V = 210$ m/min, $f = 100$ μm/rev, $a_p = 2.03$ mm)

120 to 150 μm/rev at the cutting speed of 170 m/min, such as conditions 3 and 4. It was deduced that the plastic work performed in the PSZ was enhanced because of higher force value. The numerical cutting forces were associated with the ductile failure displacement $\left(\overline{u}^{pl}\right)$ which was changed to keep the intensity of failure constant for different feeds.

The FE model was also verified through the comparison of the numerical forces with the experimental values. The differences between numerical and experimental forces were 5%, 8.1%, 1.7% and − 2% for conditions 1–4, respectively. It was obvious that the numerical forces for conventional high cutting speeds were very close to the results of the experiments.

Despite differences in terms of cutting force, this displacement-based ductile failure numerical model provides a prediction of force F_c with a good correlation.

Fe simulation in extreme high-speed machining

In order to validate whether the developed numerical approach can be employed at extreme high cutting speeds in the range $1200 \leq V \leq 4800$ m/min, the numerical results were compared with experimental ones. The cutting conditions and tool geometry were identical to those of the experiments reported in the literature [41, 42]. The orthogonal machining was simulated at relatively high cutting speeds of 1200, 2400 and 4800 m/min, feeds of 35, 42 and 70 μm/rev and depth of cut of 5 mm. The tool geometry for ISO P20 tungsten carbide was consisted of a rake angle of 0° and clearance angle of 6°.

Chip formation and morphology

Figure 11 illustrates the experimentally obtained [41] and numerically calculated chip formation at the cutting speed of 1200 m/min. It was found that the global chip morphology acquired by simulation showed a great similarity to that given in the experimental result. The plastic deformation occurred within the PSZ near the tool tip in both numerical and experimental investigations.

When the cutting speed was extremely increased, the great plastic strains were located around the shear plane extending

Fig. 10 Comparison between numerical and experimental [7] forces F_c for conventional high cutting speeds
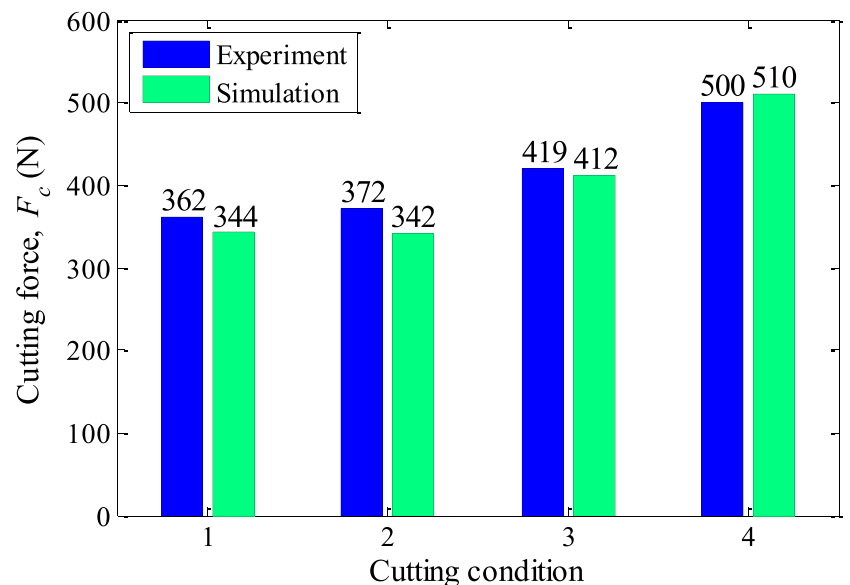
$(1: V = 210$ m/min, $f = 100$ μm/rev; $2: V = 250$ m/min, $f = 100$ μm/rev; $3: V = 170$ m/min, $f = 120$ μm/rev; $4: V = 170$ m/min, $f = 150$ μm/rev)

Fig. 11 Chip morphology of Ti-6Al-4V acquired for orthogonal machining at $V = 1200$ m/min and $f = 70$ μm/rev: (a) numerical; (b) experimental [41]
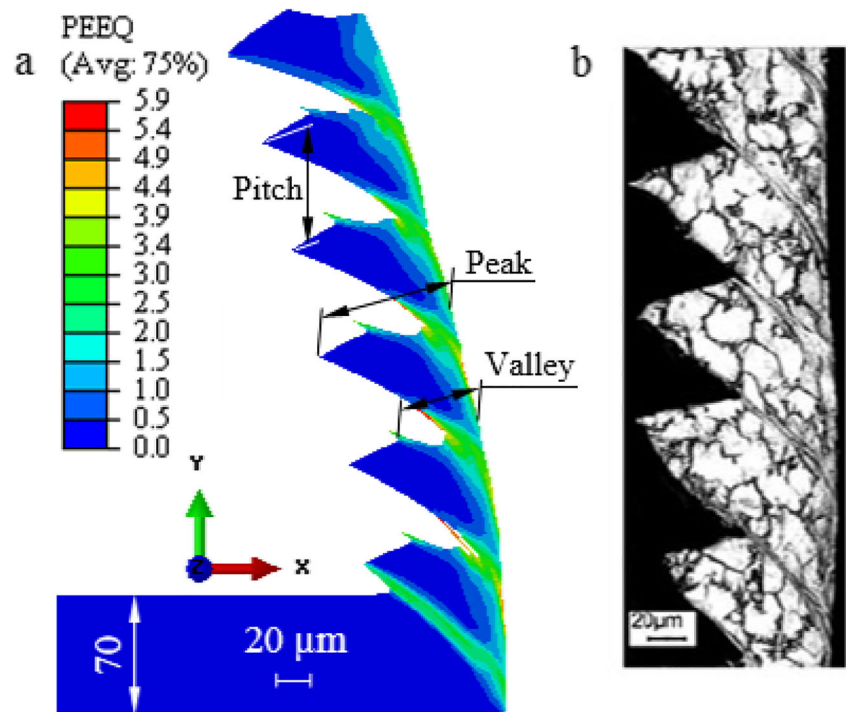
from the chip root to the external chip surface. The scale of equivalent plastic strain (PEEQ) was fixed to about 6. The

PEEQ values along the PSZ, where the severe shearing behavior was taken place, were approximately varied from 2 to 4.5.

Fig. 12 Chip serration of Ti-6Al-4V at $V = 1200$ m/min and $f = 70$ μm/rev: (a) $t = 4.375 \times 10^{-6}$ s; (b) $t = 4.9001 \times 10^{-6}$ s; (c) $t = 7 \times 10^{-6}$ s; (d) $t = 7.5251 \times 10^{-6}$ s
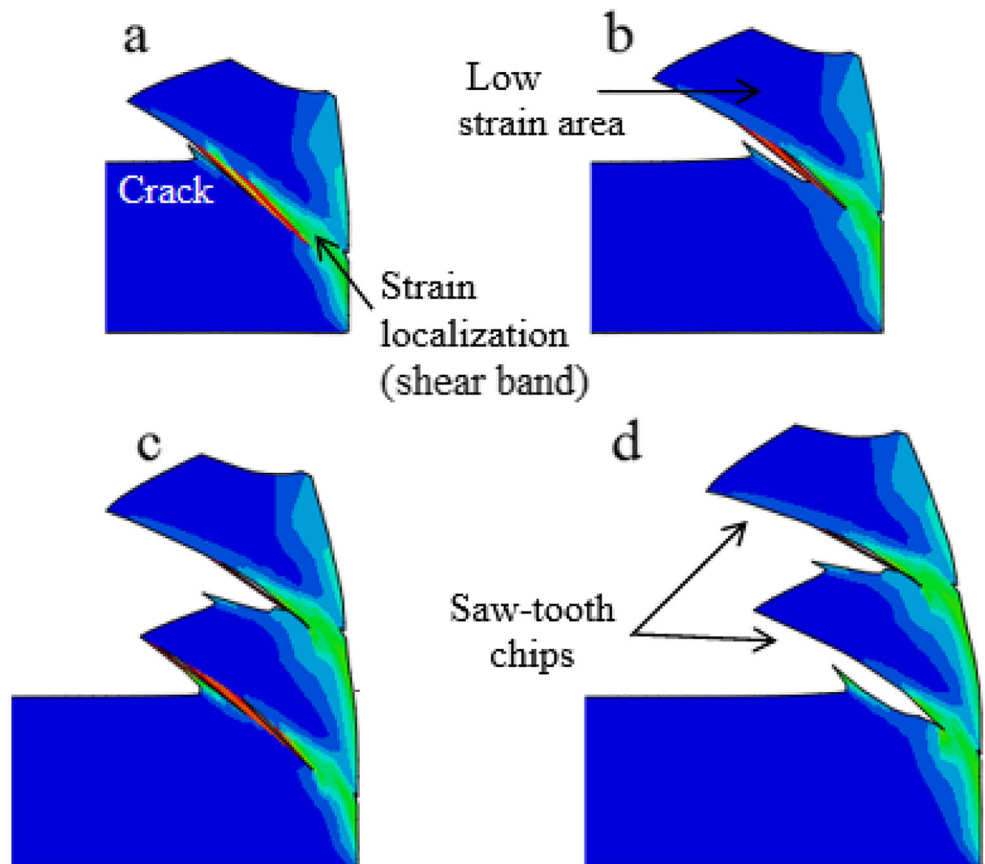
Table 6 Comparison between the characteristics of numerical and experimental [41, 42] chips in extremely high-speed machining

Cutting Conditions		Chip morphology (µm)			Frequency, f_c (kHz)
		Valley	Peak	Pitch	
V=1200 m/min	Experimental	50	106	68	444
f=70 µm/rev	Numerical	52	84	63	380
	Difference	-4%	20.8%	7.4%	14.4%
V=2400 m/min	Experimental	30	49	35	1333
f=42 µm/rev	Numerical	33	51	36	1336
	Difference	−10%	−4.1%	−2.9%	−0.2%
V=4800 m/min	Experimental	25	50	43	2631
f=35 µm/rev	Numerical	29	43	34	2869
	Difference	−16%	14%	20.9%	−9%

It was revealed from Fig. 12, where the cutting speed was much higher, that the serration of chips was initiated through gross periodic fracture which occurred in the PSZ and developed to the outer surface of the chip. When the segment was released from the crack, compressive stresses began to build up and gross fracture was taken place again in the same manner. The scalar stiffness degradation (SDEG) was greater than 0.96, which was used as the critical parameter to determine the material failure. It can be concluded that at extreme high cutting speeds, ductile fracture plays more significant role in shear-localization than thermoplastic instability, also named as adiabatic shear.

The fracture behavior generated during the simulation of extreme high-speed machining of Ti-6Al-4V was different from that obtained in conventional high-speed machining. The facture in extreme high-speed machining was located in the PSZ and would separate almost the adjacent shear bands because of increasing the strain rate in the PSZ with cutting speed while it was taken place at the external chip surface in conventional high-speed machining. Finally, the chip morphology was affected from cutting speed variation.

In both conventional and extreme high-speed machining cases, the chip segment was separated from the outer surface of the chip while joined to each other at the rake face. This indicated that the strength of the chip to the crack growth on the tool side was greater than the outer surface one.

When machining Ti-6Al-4V under severe cutting conditions, the acquired numerical and actual [41, 42] dimensions of saw-tooth chip morphology can be seen in Table 6. It was found for all the cutting speeds studied that the numerically acquired valley heights were in accordance with the experimental ones while the differences were less than about 15%. For the peak heights, all predicted results were close to experimental data with differences 20.8%, −4.1%, 14% for the cutting speeds of 1200, 2400, 4800 m/min, respectively. Also, the differences of segment pitches were not more than about 20%.

The variation of serrated frequency f_c for extreme high-speed machining conditions is presented in Table 6. For the parameters $V = 1200$ m/min and $f = 70$ µm/rev, the frequency value found numerically was approximately 380 kHz. This result was almost close to that acquired experimentally (444 kHz). It was also concluded that the frequency values calculated from the numerical simulations matched well with those acquired from the actual measurements on the chip.

Cutting force

In the case of a cutting speed of 1200 m/min and feed of 70 µm/rev, the variation of the predicted force F_c with time is shown in Fig. 13. The force fluctuation occurred periodically due to the chip serration, but there was not severe fluctuation. As mentioned previously, the scale of PEEQ was set to about 6. Therefore, the elements having greater distortion (PEEQ>6) can be ignored.
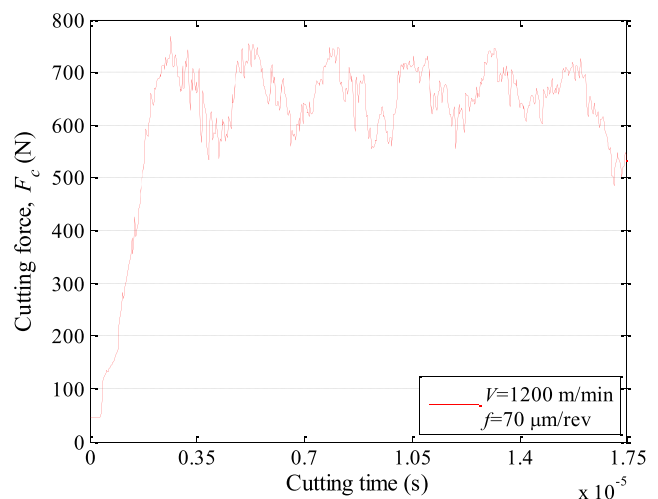

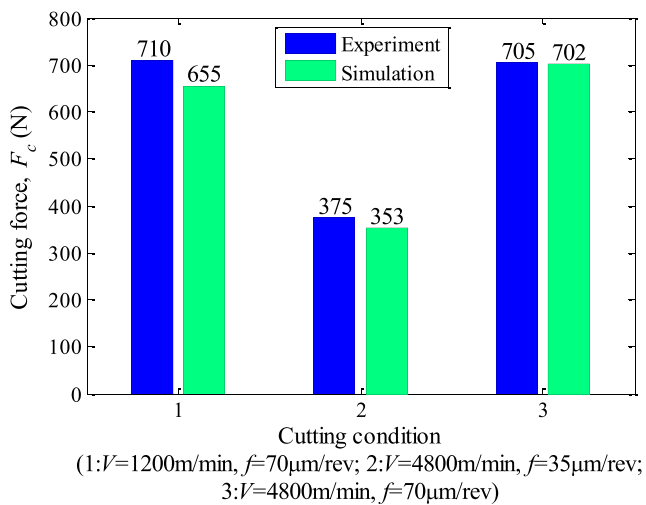**Fig. 13** Variation in the numerical force F_c with time (V = 1200 m/min, f = 70 µm/rev, a_p = 5 mm)

Fig. 14 Comparison between numerical and experimental [41] forces F_c for extreme high cutting speeds

Figure 14 illustrates the average numerical and experimental [41] forces F_c acquired in extremely high-speed machining. The force F_c calculated at the cutting speed of 1200 m/min and feed of 70 μm/rev was slightly underestimated. However, this numerical result was acceptable. For the higher cutting speed of 4800 m/min and feed of 70 μm/rev, the numerical force F_c was very close to the experimental result. These results indicated that the principal cutting forces predicted through the newly developed numerical approach were in agreement with the actual values, even if the cutting speed was much higher. It can be also deduced that the difference between the experimental and numerical results becomes lesser due to an increase in cutting speed.

Conclusions

In this study, the FE-based numerical model of orthogonal machining was suggested to analyze the high-speed machining process of Ti-6Al-4V. For the multi-part numerical approach, material behavior and failure criterion were represented through the JC law. The following findings were drawn:

- I n high-speed cutting, the saw-tooth chip occurred with ductile fracture, arising from a thermal softening mechanism in the PSZ.
- The crack, which produced the saw-tooth chip segment, was initiated at the external chip surface under conventional high cutting speed, and developed toward the tool tip. Due to the thermal softening mechanism, there was not crack on the tool side.
- In machining of Ti-6Al-4V at extreme high cutting speed, the fracture was occurred in the PSZ. This can be related to the formation of great plastic strains in the PSZ.
- The FE model using the JC material law along with a displacement-based ductile failure and no remeshing

technique was able to accurately calculate the chip morphology and cutting force over a range of conventional high cutting speeds, and provided a reasonable prediction of the chip characteristics by keeping constant intensity of failure for different feeds. Besides, a similar plastic deformation in shear bands was seen in both numerical and experimental investigations. Therefore, ductile failure criterion was suitable for high-speed machining of Ti-6Al-4V.

- The numerical chip morphology and cutting force agreed well with actual values, even with a quite great variation of cutting speed. It was inferred that the presented FE model was successfully utilized to model the orthogonal machining of Ti-6Al-4V and calculate satisfactorily the chip morphology and the cutting force.
- In conventional high-speed machining, the numerical cutting forces were slightly influenced from the increase in the cutting speed. Also, the cutting force changed significantly with increasing feed at a given cutting speed.
- A positive correlation was observed between the numerical and experimental frequencies of saw-tooth chips. The numerical serrated frequencies also indicated an increase tendency with increasing cutting speed, especially at conventional high speeds.

Declaration

References

1. Molinari A, Musquar C, Sutter G (2002) Adiabatic shear banding in high speed machining of Ti-6Al-4V: experiments and modeling. Int J Plast 18(4):443–459
2. Che-Haron CH, Jawaid A (2005) The effect of machining on surface integrity of titanium alloy Ti–6%Al–4%V. J Mater Process Technol 166(2):188–192
3. Calamaz M, Coupard D, Girot F (2008) A new material model for 2D numerical Sim-ulation of serrated chip formation when machining titanium alloy Ti-6Al-4V. Int J Mach Tools Manuf 48(3-4):275–288
4. Gao C, Zhang L (2013) Effect of cutting conditions on the serrated chip formation in high-speed cutting. Mach Sci Technol 17(1):26–40
5. Johnson GR, Cook WH (1983) A constitutive model and data for metals subjected to large strains, high strain rate, and temperatures. In: Proceedings of the international symposium on ballistics, The Hague, The Netherlands, pp. 1–7
6. Vaziri MR, Salimi M, Mashayekhi M (2011) Evaluation of chip formation simulation models for material separation in the presence of damage models. Simul Model Pract Th 19(2):718–733
7. Chen G, Ren CZ, Yang XY, Jin XM, Guo T (2011) Finite element simulation of high-speed machining of titanium alloy (Ti-6Al-4V)

based on ductile failure model. Int J Adv Manuf Technol 56(9-12): 1027–1038

8. Ali MH, Ansari MNM, Khidhir BA, Mohamed B, Oshkour AA (2014) Simulation machining of titanium alloy (Ti-6Al-4V) based on the finite element modeling. J Braz Soc Mech Sci Eng 36(2): 315–324

9. Aydin M (2017) Prediction of cutting speed interval of diamond-coated tools with residual stress. Mater Manuf Process 32(2):145–150

10. Aydın M, Köklü U (2017) Identification and modeling of cutting forces in ball-end milling based on two different finite element models with arbitrary Lagrangian Eulerian technique. Int J Adv Manuf Technol 92(1-4):1465–1480

11. Jain A, Khanna N, Bajpai V (2018) FE simulation of machining of Ti-54M titanium alloy for industry relevant outcomes. Measurement 129:268–276

12. Calamaz M, Coupard D, Girot F (2010) Numerical simulation of titanium alloy dry machining with a strain softening constitutive law. Mach Sci Technol 14(2):244–257

13. Calamaz M, Coupard D, Nouari M, Girot F (2011) Numerical analysis of chipformation and shear localisation processes in machining the Ti-6Al-4V titanium alloy. Int J Adv Manuf Technol 52(9-12): 887–895

14. Sima M, Özel T (2010) Modified material constitutive models for serrated chip formation simulations and experimental validation in machining of titanium alloy Ti-6Al-4V. Int J Mach Tools Manuf 50(11):943–960

15. Ning J, Liang SY (2018) Model-driven determination of Johnson-Cook material constants using temperature and force measurements. Int J Adv Manuf Technol 97(1-4): 1053–1060

16. Ning J, Nguyen V, Huang Y, Hartwig KT, Liang SY (2018) Inverse determination of Johnson–Cook model constants of ultra-fine-grained titanium based on chip formation model and iterative gradient search. Int J Adv Manuf Technol 99(5-8):1131–1140

17. Umbrello D (2008) Finite element simulation of conventional and high speed machining of Ti6Al4V alloy. J Mater Process Technol 196(1-3):79–87

18. Subbiah S, Melkote SN (2008) Effect of finite edge radius on ductile fracture ahead of the cutting tool edge in micro-cutting of Al2024-T3. Mater Sci Eng A 474(1-2):283–300

19. Owen DRJ, Vaz JM (1999) Computational techniques applied to high-speed machining under adiabatic strain localization conditions. Comput Methods Appl Mech Eng 171:445–461

20. Wang B, Liu Z (2014) Investigations on the chip formation mechanism and shear localization sensitivity of high-speed machining Ti6Al4V. Int J Adv Manuf Technol 75(5-8): 1065–1076

21. Ambati R, Yuan H (2011) FEM mesh-dependence in cutting process simulations. Int J Adv Manuf Technol 53(1-4):313–323

22. Mabrouki T, Girardin F, Asad M, Rigal JF (2008) Numerical and experimental study of dry cutting for an aeronautic aluminium alloy. Int J Mach Tools Manuf 48(11):1187–1197

23. Zhang YC, Mabrouki T, Nelias D, Gong YD (2011) Chip formation in orthogonal cutting considering interface limiting shear stress and damage evolution based on fracture energy approach. Finite Elem Anal Des 47(7):850–863

24. Hua J, Shivpuri R (2004) Prediction of chip morphology and segmentation during the machining of titanium alloys. J Mater Process Technol 150(1-2):124–133

25. Sutter G, List G (2013) Very high speed cutting of Ti-6Al-4V titanium alloy-change in morphology and mechanism of chip formation. Int J Mach Tools Manuf 66:37–43

26. Ducobu F, Rivière-Lorphèvre E, Filippi E (2015) Experimental contribution to the study of the Ti6Al4V chip formation in orthogonal cutting on a milling machine. Int J Mater Form 8(3):455–468

27. Singh BK, Roy H, Mondal B, Roy SS, Mandal N (2019) Measurement of chip morphology and multi criteria optimization of turning parameters for machining of AISI 4340 steel using Y-ZTA cutting insert. Measurement 142:181–194

28. Wang B, Liu Z (2016) Evaluation on fracture locus of serrated chip generation with stress triaxiality in high speed machining of Ti6Al4V. Mater Des 98:68–78

29. Jomaa W, Mechri O, Lévesque J, Songmene V, Bocher P, Gakwaya A (2017) Finite element simulation and analysis of serrated chip formationduring high–speed machining of AA7075–T651 alloy. J Manuf Process 26:446–458

30. Wan L, Wang D (2015) Numerical analysis of the formation of the dead metal zone with different tools in orthogonal cutting. Simul Model Pract Th 56:1–15

31. Shuang F, Chen X, Ma W (2018) Numerical analysis of chip formation mechanisms in orthogonal cutting of Ti6Al4V alloy based on a CEL model. Int J Mater Form 11(2):185–198

32. Zhao W, Yang Q, Khan AM, He N, Zhang A (2019) An inverse-identification-based finite element simulation of orthogonal cutting tungsten carbide. J Braz Soc Mech Sci Eng 41(2):85

33. Aydın M, Köklü U (2020) Analysis of flat-end milling forces considering chip formation process in high-speed cutting of Ti6Al4V titanium alloy. Simul Model Pract Th 100: 102039

34. Johnson GR, Holmquist TJ (1989) Test data and computational strengthen and fracture model constants for 23 materials subjected to large strain, high-strain rates, and high temperatures, LA-11463-MS, Los Alamos National laboratory

35. Mabrouki T, Rigal JF (2006) A contribution to a qualitative understanding of thermo-mechanical effects during chip formation in hard turning. J Mater Process Technol 176(1-3):214–221

36. Johnson GR (1981) Dynamic analysis of a torsion test specimen including heat conduction and plastic flow. J Eng Mater Technol 103(3):201–206

37. Zorev NN (1963) Inter-relationship between shear processes occurring along tool face and shear plane in metal cutting. In: International Research in Production Engineering ASME, New York, pp. 42–49

38. Arrazola PJ, Villar A, Ugarte D, Marya S (2007) Serrated chip prediction in finite element modeling of the chip formation process. Mach Sci Technol 11:367–390

39. Thepsonthi T, Özel T (2015) 3-D finite element process simulation of micro-end milling Ti-6Al-4V titanium alloy: experimental validations on chip flow and tool wear. J Mater Process Technol 221:128–145

40. Vyas A, Shaw MC (1999) Mechanics of saw–tooth chip formation in metal cutting. J Manuf Sci Eng 121(2):163–172

41. Gente A, Hoffmeister HW (2001) Chip formation in machining Ti6Al4V at extremely cutting speed. CIRP Ann Manuf Technol 50(1):49–52

42. Bäker M, Rösler J, Siemers C (2002) A finite element model of high speed metal cutting with adiabatic shearing. Comput Struct 80(5-6): 495–513